ADVANCED MATERIALS
www.advmat.de

Electrode-Induced Self-Healed Monolayer MoS_2 for High Performance Transistors and Phototransistors

Sangyeon Pak, Seunghun Jang, Taehun Kim, Jungmoon Lim, Jae Seok Hwang, Yuljae Cho, Hyunju Chang, A-Rang Jang, Kyung-Ho Park, John Hong, and SeungNam Cha**

Contact engineering for monolayered transition metal dichalcogenides (TMDCs) is considered to be of fundamental challenge for realizing high-performance TMDCs-based (opto) electronic devices. Here, an innovative concept is established for a device configuration with metallic copper monosulfide (CuS) electrodes that induces sulfur vacancy healing in the monolayer molybdenum disulfide (MoS_2) channel. Excess sulfur adatoms from the metallic CuS electrodes are donated to heal sulfur vacancy defects in MoS_2 that surprisingly improve the overall performance of its devices. The electrode-induced self-healing mechanism is demonstrated and analyzed systematically using various spectroscopic analyses, density functional theory (DFT) calculations, and electrical measurements. Without any passivation layers, the self-healed MoS_2 (photo)transistor with the CuS contact electrodes show outstanding room temperature field effect mobility of 97.6 cm^2 $(Vs)^{-1}$, On/Off ratio > 10^8, low subthreshold swing of 120 mV per decade, high photoresponsivity of 1×10^4 A W^{-1}, and detectivity of 10^{13} jones, which are the best among back-gated transistors that employ 1L MoS_2. Using ultrathin and flexible 2D CuS and MoS_2, mechanically flexible photosensor is also demonstrated, which shows excellent durability under mechanical strain. These findings demonstrate a promising strategy in TMDCs or other 2D material for the development of high performance and functional devices including self-healable sulfide electrodes.

1. Introduction

Monolayered transition metal dichalcogenides (TMDCs) have great potential in developing next-generation flexible, transparent, and wearable electronics and optoelectronics due to their reduced dimensions that offer flexibility and transparency with proper band gap, high carrier mobility, and highly efficient light absorption.[1–3] In addition, their ideally dangling-bond-free surface and atomic thickness are promising for ideal heterogeneous contact and reduced short channel effect,[4] thus making them suitable for future nano-scaled electronic and optoelectronic devices. An ideal field-effect transistor based on an molybdenum disulfide (MoS_2) channel is theoretically predicted to reach large on/off ratio (>10^9), room temperature mobility of 410 cm^2 $(Vs)^{-1}$, and near-ideal subthreshold swing of 60 meV per decade.[5,6] However, most of experimental results significantly differ from the aforementioned theoretical predictions. One of dominant factors degrading the overall performance of 2D materials based devices arises from unwanted chemical interactions between deposited metal electrodes and 2D TMDC channel. These chemical interactions originate from incomplete/imperfect covalent/surface bonds of TMDCs and unwanted damages from the direct deposition of metal layers and precursors, which are used during the device fabrication processes. These lead to the creation of unfavorable interface states and pinning of fermi energy levels, which

S. Pak, T. Kim, J. Lim, S. Cha
Department of Physics
Sungkyunkwan University (SKKU)
Suwon, Gyeonggi-do 16419, Republic of Korea
E-mail: chasn@skku.edu
S. Jang, H. Chang
Chemical Data-Driven Research Center
Korea Research Institute of Chemical Technology (KRICT)
Gajeong-ro 141, Daejeon 34114, Republic of Korea
J. S. Hwang, K.-H. Park
Nanodevices Laboratory
Korea Advanced Nano Fab Center (KANC)
Suwon 16229, Republic of Korea
The ORCID identification number(s) for the author(s) of this article can be found under https://doi.org/10.1002/adma.202102091.
Y. Cho
University of Michigan - Shanghai Jiao Tong University Joint Institute
Shanghai Jiao Tong University
Minhang District, Shanghai 200240, P. R. China
A.-R. Jang
Department of Electrical Engineering
Semyung University
Chungcheongbuk-do 27136, Republic of Korea
J. Hong
School of Materials Science and Engineering
Kookmin University
Seoul 02707, Republic of Korea
E-mail: johnhong@kookmin.ac.kr

DOI: 10.1002/adma.202102091

increase the contact energy barriers and contact resistances, hence impacting the overall electronic and optoelectronic device performance of 2D TMDCs based devices. Thus, it has been desired to find appropriate contact materials and device fabrication methods that can improve the interface properties between 2D TMDCs and electrode materials.

In this regard, various device fabrication strategies have been proposed to realize clean and atomically sharp metal-TMDC interface properties such as insertion of graphene or hexagonal boron nitride layers,[7] dry transferring of metal layers,[8] assembly of substitutionally doped TMDCs,[9] employment of indium contacts,[10] and phase engineered MoS_2.[11] In each case, fabrication processes led to mitigate the partial Fermi level pinning effects and lowered the nontrivial Schottky contact barriers. Nevertheless, such processes require an additional fabrication steps that are difficult to control and/or lead to unwanted chemical interactions that could possibly change inherent characteristics of the TMDC channel materials. Furthermore, anion defects in monolayered TMDCs are naturally built during its high-temperature synthesis or fabrication/transfer steps, resulting in irregular electrical properties upon the device location of a wafer or material preparation methods. It is thus expected to find new electrode system that can not only induce low contact barriers for efficient charge transport but also produce uniform electronic properties of TMDC monolayers.

In this work, we present an innovative, self-healed electrode system that employ metallic copper monosulfide (CuS) electrodes to fabricate high performance transistors and phototransistors based on a chemical vapor deposition (CVD)-grown MoS_2 monolayer. We demonstrate that the excess sulfur adatoms from the CuS electrodes provide electrode-induced sulfur vacancy self-healing (SVSH) and reduce defect sites within the MoS_2 channel and the MoS_2/CuS interface. Furthermore, the SVSH mechanism was explained through surface energy barrier calculation by density functional theory (DFT) that supports the thermodynamically favorable reactions of sulfur adatoms healing on the sulfur vacancies in the MoS_2 channel. Without any passivation layers, the MoS_2/CuS electronic device reached room temperature field effect mobility of 97.6 cm^2 $(Vs)^{-1}$, On/Off ratio > 10^8, and low subthreshold swing of 120 mV per decade in a back-gated transistor configuration, which are highest among reported values for back-gated transistors with CVD-grown MoS_2 monolayers.[1,12–18] In addition, the MoS_2/CuS phototransistor showed high photoresponsivity of 1×10^4 A W^{-1} and detectivity of 10^{13} jones, which is among the highest reported values for MoS_2-based photodetectors. We further fabricated the two-terminal flexible photodetector to show excellent durability under applied bending strain due to the ultrathin nature and outstanding flexibility of the CuS electrodes and MoS_2 monolayer. These findings and development in new CuS contact electrodes pave a powerful strategy to provide CuS electrode-based future electronics and optoelectronics based on 2D TMDC materials.

2. Results and Discussions

Conductive and transparent copper sulfide (CuS) nanosheet films were prepared by a facile, one-step sulfurization method of Cu metal films (10 nm) which was deposited using a thermal evaporation technique as shown in the schematics and optical image of **Figure 1**a. Note that the Cu metal films were directly exposed to H_2S gas under ambient condition at room temperature to synthesize CuS nanosheet films as we previously reported.[19] Reactive H_2S gases adsorb onto Cu surface and donate sulfur ions, and copper corrosion reaction with adsorbed sulfur ions leads to the formation of covellite CuS structure. In spite of the ultrathin thickness of CuS, its electrical properties are known to be as good as indium tin oxide (see Figure S1, Supporting Information, for electrical data).[19] The synthesized CuS nanosheet films possess covellite structure (JCPDS card No. 78–0877) as confirmed by the XRD analysis (Figure 1b). The Raman spectrum of CuS shows distinct Raman vibrational modes at around 263.8 and 471.3 cm^{-1}, which correspond to the lattice Cu—S and S—S stretching of covellite, respectively (Figure S2, Supporting Information).[19]

The MoS_2/CuS transistor was fabricated by transferring the CuS nanosheet films onto the MoS_2 monolayer (Figure 1c). Polystyrene (PS) films were used to detach the CuS/PS films in deionized (DI) water,[20,21] and the films were dried in air to completely remove water molecules to achieve clean interface between the CuS electrodes and MoS_2 monolayers. Then, the PS films were attached onto the substrate that has the MoS_2 monolayers. To observe and confirm that the CuS electrodes are well attached onto the monolayers of MoS_2, we first performed Raman and photoluminescence (PL) analysis of the MoS_2/CuS heterostructure. Figure 1d shows Raman spectrum of the MoS_2 monolayer (black line) and the MoS_2/CuS heterostructure (red line). The Raman spectra of the vertically stacked heterostructure consists of the distinctive Raman peaks of CuS and MoS_2 layers, implying the formation of the MoS_2/CuS heterostructure. The PL spectra (Figure 1e) obtained from the MoS_2 monolayer and the MoS_2/CuS heterostructure shows a distinctive emission peak at the characteristic direct exitonic energy at 1.88 eV ($\lambda \approx 660$ nm). Also, it is noticed that there was a significant reduction in the PL intensity for the MoS_2/CuS heterostructure. The reduced PL intensity can be attributed to the exciton dissociation (Figure 1f) and charge transfer associated with the formation of metal (CuS)–semiconductor (MoS_2) junction.

The CuS electrode induced SVSH of MoS_2 channel was achieved through mild thermal annealing at 150 °C in a vacuum chamber as depicted in **Figure 2**a. Note that only sulfur adatoms are involved during this process, and unreacted H_2S gas does not present within the surface of CuS crystal. The SVSH mechanism is that the excess sulfur adatoms from the CuS electrodes (TEM-EDS spectrum can be found in Figure S3, Supporting Information) are diffused through the MoS_2 channel, and its defect sites (e.g., sulfur vacancies) are healed spontaneously by thermodynamically favorable adsorption/binding of the sulfur adatoms.[22,23] Note that vacancy healing have been previously proposed using chemical treatments to enhance the PL intensity in monolayered TMDCs.[24–26] However, the proposed mechanism was sorely focused on the monolayers themselves and chemical treatments, and the self-healing using device electrodes is not yet explored. To confirm analytically the SVSH mechanism, we first employed XPS analysis as shown in Figure 2b. The XPS spectra shows Mo 3d orbital (Mo^{+4} $3d_{5/2}$

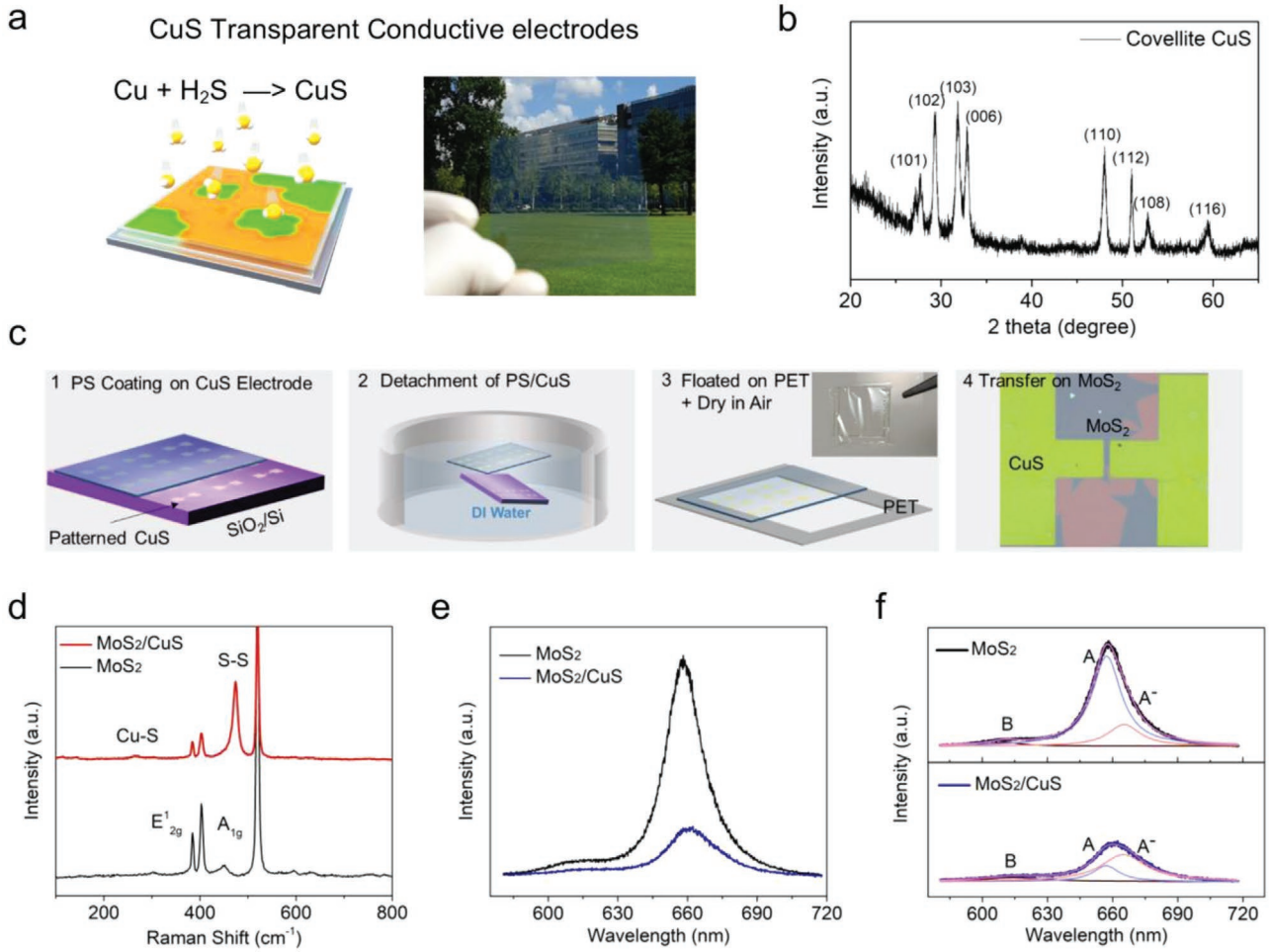

Figure 1. Synthesis and characterization of CuS and MoS_2/CuS hybrid structure. a) A schematic illustration and optical image of the CuS film synthesized using H_2S gas and Cu film b) X-ray diffraction pattern of CuS nanosheet. c) Fabrication procedures of MoS_2/CuS hybrid structure using polymer-assisted transfer method. d) Raman and e) photoluminescence spectrum of MoS_2 and MoS_2/CuS hybrid structure. f) Deconvolution of the PL spectra to identify the relative contribution from trions (A^-) and exciton (A) by fitting with Lorentzian curves.

and Mo^{+4} $3d_{3/2}$) of the as-grown MoS_2 and the MoS_2/CuS heterostructure. The deconvoluted peaks can be assigned to intrinsic MoS_2 (i-MoS_2, 230.08 eV and 233.23 eV) and defective MoS_2 (d-MoS_2, 229.83 eV and 232.98 eV).[22,27] When the as-grown MoS_2 monolayer is healed by the sulfur adatoms from the CuS electrodes, the peak contribution from the i-MoS_2 is increased, whereas the d-MoS_2 is decreased, resulting in the shift of the doublets to the higher binding energy. The XPS spectra of S 2p also confirms the SVSH mechanism (Figure S4, Supporting Information).[22,28]

The SVSH mechanism was also confirmed using annular dark field scanning tunneling electron microscope (ADF-STEM) measurement, and the direct vision of the atomic structure were obtained for pristine MoS_2 and MoS_2/CuS heterostructure as shown in Figure 2c and d, respectively. The STEM images of the pristine MoS_2 crystals clearly showed the spatial distribution of the Mo and S atoms, and the Mo atoms appear brighter than the S atoms. As shown in Figure 2c, the vacancy sites of S atoms in pristine MoS_2 are darker than the Mo and S atoms. On the contrary, the self-healed MoS_2 (Figure 2d) displayed uniform atomic arrangement, which implicates that the SVSH by the CuS electrodes can effectively decrease the sulfur vacancies in the monolayered MoS_2.

To further elucidate the CuS-induced SVSH mechanism and the effect of SVSH, the PL spectrum was obtained from the overlapped CuS/MoS_2 regions (region 1- CuS/MoS_2, region 2 and 3- MoS_2 in the inset image) as shown in Figure 2e, and the PL intensity mapping image can be seen in Figure S5, Supporting Information. The PL intensity of MoS_2 at the region 1 is largely decreased due to the formation of metal-semiconductor junction. On the contrary, at the region 2 and 3, the PL intensity was largely increased. The PL intensities are even higher than that of as-grown monolayered MoS_2. Such changes in the PL intensity are attributed to the CuS-induced vacancy healing, and such healing trends were also confirmed previously, where the PL quantum efficiency of MoS_2 was enhanced due to the reduced number of defect sites and the consequent nonradiative recombination within the MoS_2 crystals.[25,27]

The energy band alignment of the MoS_2 and CuS electrodes before and after the thermal annealing have been

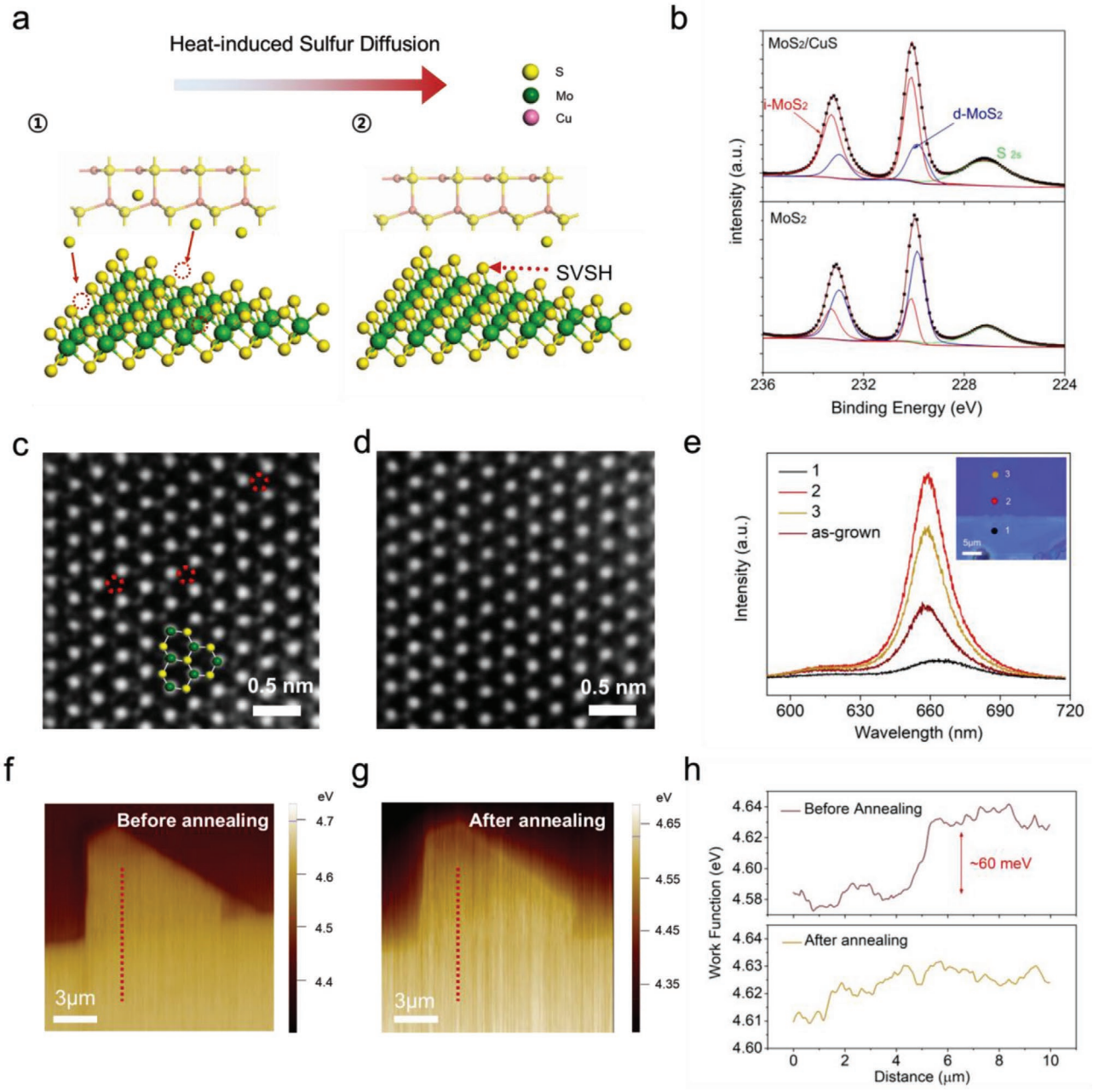

Figure 2. Sulfur-vacancy self-healing mechanism in the MoS_2/CuS hybrid structure. a) A schematic illustration of the annealing-induced self-healing of sulfur vacancies in MoS_2. b) X-ray photoelectron spectroscopy measurement of Mo 3d orbital in MoS_2 and MoS_2/CuS structure. ADF-STEM images of c) pristine MoS_2 and d) the self-healed MoS_2. e) PL spectrum taken from the points in the optical image (inset). f,g) Kelvin probe force microscopy 2D mapping image of the MoS_2/CuS hybrid structure. h) KPFM line profile taken from the images in (f,g).

further probed by a kelvin probe force microscope (KPFM) to verify the effect of the SVSH on the energy levels of MoS_2. It should be noted that surface/interface defect states are known to affect the energy level offset and alignment between the electrodes and the channel. Reduced sulfur vacancy sites can also lower the contact energy barriers and induce the efficient charge transfer.[29,30] The 2D work function mapping at the CuS/MoS_2 heterostructure was obtained before and after the thermal annealing process (Figure 2f,g). The KPFM images represent the noticeable band offset between the MoS_2 and CuS electrodes junction before the annealing process, while the difference in the work function is relatively decreased after the annealing process, as observed by the color difference and small energy depth on the line profiles (Figure 2h) which are directly extracted from the KPFM mapping images in Figure 2f,g. Also, the work function of CuS and MoS_2 is slightly changed possibly due to the desorption of oxygen/water molecules[31] and/or diffusion of sulfur adatoms from CuS to MoS_2. The work function line profiles clearly show, before the annealing process, a noticeable intrinsic band

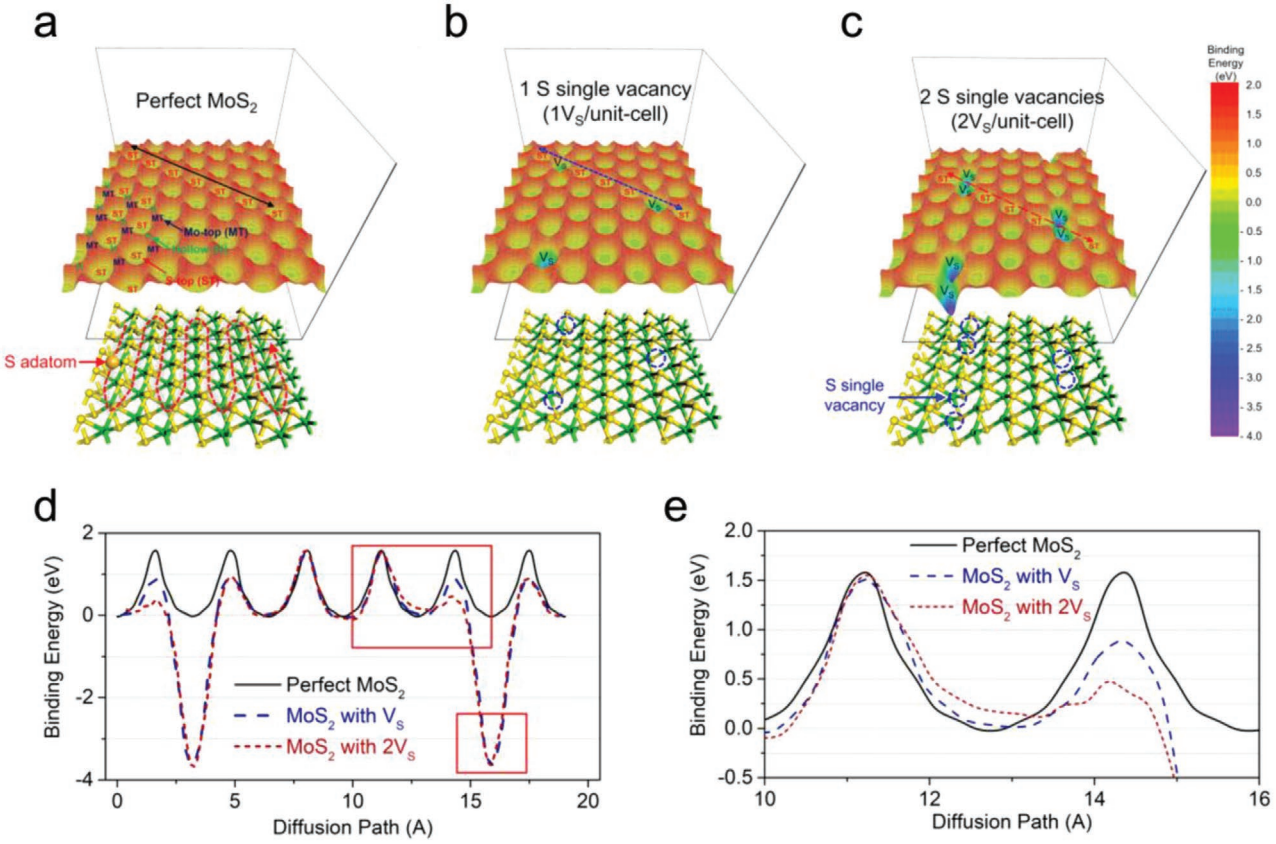

Figure 3. Binding energy surfaces (BESs) of a sulfur adatom on perfect and defective MoS_2 surfaces. BESs of a sulfur adatom placed in different positions (upper) and optimized atomic surface structures (lower) on a) perfect MoS_2, b) MoS_2 with sulfur single vacancy, c) MoS_2 with neighboring sulfur vacancies. The yellow and green spheres represent sulfur and molybdenum atoms, respectively. As displayed by the wavy red arrows in the lower figure of (a), BESs were calculated by moving the position of a sulfur adatom on the perfect and defective MoS_2 surfaces. The blue circles in the lower figures of (b) and (c) imply the locations of the sulfur single vacancies. d) Energy barrier profiles for proposed surface diffusion paths (double-headed arrows in (a–c) of a sulfur adatom. e) Encircled view of energy barrier profile corresponding to the hollow rectangular part in figure of (d).

offset around 60 meV and the corresponding depletion region between the MoS_2 monolayer and CuS electrodes. After the mild thermal annealing, the band offset is relatively reduced as well as the depletion region. The contact energy barriers between the MoS_2 monolayer and CuS electrodes are reduced due to the SVSH mechanism, which is in accordance with the XPS, STEM, and PL results.

To further support our claim that the sulfur adatoms can favorably heal the sulfur vacancies in MoS_2, we calculated the binding energy surfaces (BESs) of sulfur adatoms in different positions over the various (perfect and defective) MoS_2 surfaces by using first-principles calculations (see Experimental Section for details). The BESs were calculated by moving the position of the sulfur adatom on each point of the different MoS_2 surface states as depicted in the lower image of **Figure 3**a. We intentionally modelled the several types of the sulfur vacancies states including a sulfur single vacancy (V_S), two neighboring sulfur single vacancies ($2V_S$), two neighboring sulfur double vacancies ($2V_{S2}$), and V_S with a sulfur adatoms (S_A) (Figure 3a–c; Figure S6, Supporting Information). The binding energy was defined as $E_{bind} = E_{S\text{-adatom/Surface}} - (E_{S\text{-adatom}} + E_{Surface})$, where $E_{S\text{-adatom/Surface}}$ is the total energy of the total system that the sulfur adatom is adsorbed on the particularly modelled surface, and $E_{S\text{-adatom}}$ and $E_{Surface}$ are the total energies of the isolated S atom and modelled surface (perfect and defective MoS_2 surfaces), respectively. For the perfect MoS_2 surface, the color map distribution of the BES of the sulfur adatoms correspond to the atomic arrangement of Mo-top (MT), S-top (ST), and hollow (H) sites (upper, Figure 3a), which are in good agreement with the atomic geometry of MoS_2. When sulfur vacancies are introduced, noticeable drop (blue puddles) in the binding energy was monitored as clearly distinguished in color map of Figure 3b,c. The binding energy of the sulfur adatom at the sulfur vacancy in MoS_2 is calculated to be around −3.7 eV, regardless of the types of vacancy states, suggesting that the adsorption of sulfur adatoms on the sulfur vacancy sites is thermodynamically spontaneous and favorable. These results are also in good agreement with the previously reported results, in which the excess oxygen adatoms can favorably attached on the sulfur vacancies in MoS_2.[32] It should be also noted that the adsorption energy of sulfur adatoms on the sulfur vacancy sites is much higher than the desorption energy of sulfur adatoms from CuS surface, suggesting that the desorption and diffusion process is likely to happen energetically under the concentration gradient and mild thermal annealing (Figure S7, Supporting Information).

Furthermore, the changes in the surface diffusion energy barrier around the sulfur vacancy sites were calculated. Figure 3d shows the diffusion energy barrier profiles extracted from proposed surface diffusion paths (double-headed arrows in a–c, a combination of ST-ST-ST or ST-V_S-ST). In the perfect MoS_2 surface, the calculated diffusion energy barrier was found to be ≈1.6 eV along with the diffusion pathway presented in Figure 3d. When the sulfur adatom is placed around the sulfur vacancy, the surface diffusion energy barrier on the MoS_2 surface with the sulfur single vacancy ($1V_S$/unit-cell) decreases to ≈0.9 eV compared to that of the perfect MoS_2 surface. In the case of the MoS_2 surface with the two neighboring sulfur single vacancies ($2V_S$/unit-cell), the reduction of diffusion energy barrier is more volatile (the calculated diffusion energy barrier on 2Vs is 0.4 eV, Figure 3e). Additionally, the effect of the diffusion energy barrier on the presence of S2 double vacancies (V_{2S}/unit-cell) or additional sulfur adatom (S_A) was also checked as shown in Figure S6, Supporting Information. In the both cases, the diffusion energy barrier reaches to the ≈0.7 and 0.9 eV, which shows the similar reduction behavior (Figure 3b,c). Lowering both binding energy surface and diffusion energy barrier within the sulfur vacancy sites confirms that the excess sulfur adatoms from the CuS electrode can favorably diffuse across the surface of MoS_2 as well as bind and heal the sulfur defect sites in MoS_2.

To understand in detail how the SVSH mechanism affects the electrical properties of MoS_2, we have fabricated MoS_2/CuS field effect transistors (FETs) on an HfO_2/Si substrate and the electrical properties of 20 control-devices were carefully examined before and after the thermal annealing process. The schem atic picture of the MoS_2/CuS FET is depicted in **Figure 4**a. Figure 4b presents the representative drain current as a function of the gate voltage, which is shown in a logarithmic scale at drain voltages of V_{ds} = 0.1, 0.3, 0.5 V, and Figure 4c shows the drain–source current as a function of the drain–source voltage on a linear scale for the as-fabricated and self-healed MoS_2/CuS FETs. The both as-fabricated and self-healed FETs exhibit the n-type characteristics, steep subthreshold swing, low off currents, high on currents, and ohmic contact as observed in the transfer and output curves, indicating that the CuS electrodes can be well applied for the metal-semiconductor contact and the low electron barrier with the MoS_2 channel. From the transfer characteristics, we estimated a field effect mobility using $\mu_{FE} = \frac{L}{WC_{ox}V_{ds}}\frac{dI_{ds}}{dV_{gs}}$, where L and W are channel length and width, C_{ox} is the gate capacitance of 309.9 nF cm^{-2}. After the thermal annealing, the room temperature, back-gated field-effect mobility of MoS_2/CuS FET is surprisingly increased from 32 to 97.6 cm^2 V^{-1} s^{-1}, which demonstrate about the threefold improvement in its mobility. Furthermore, the self-healed MoS_2/CuS FET showed noticeable improvement in the On/Off ratio and subthreshold swing value as shown in Figure 4b and d. The On/Off current ratio is increased from 10^6 to >10^8 upon mild thermal annealing. Furthermore, the subthreshold swing values of the self-healed MoS_2/CuS FETs were decreased by 33% and reached the value as low as 120 mV per decade in a

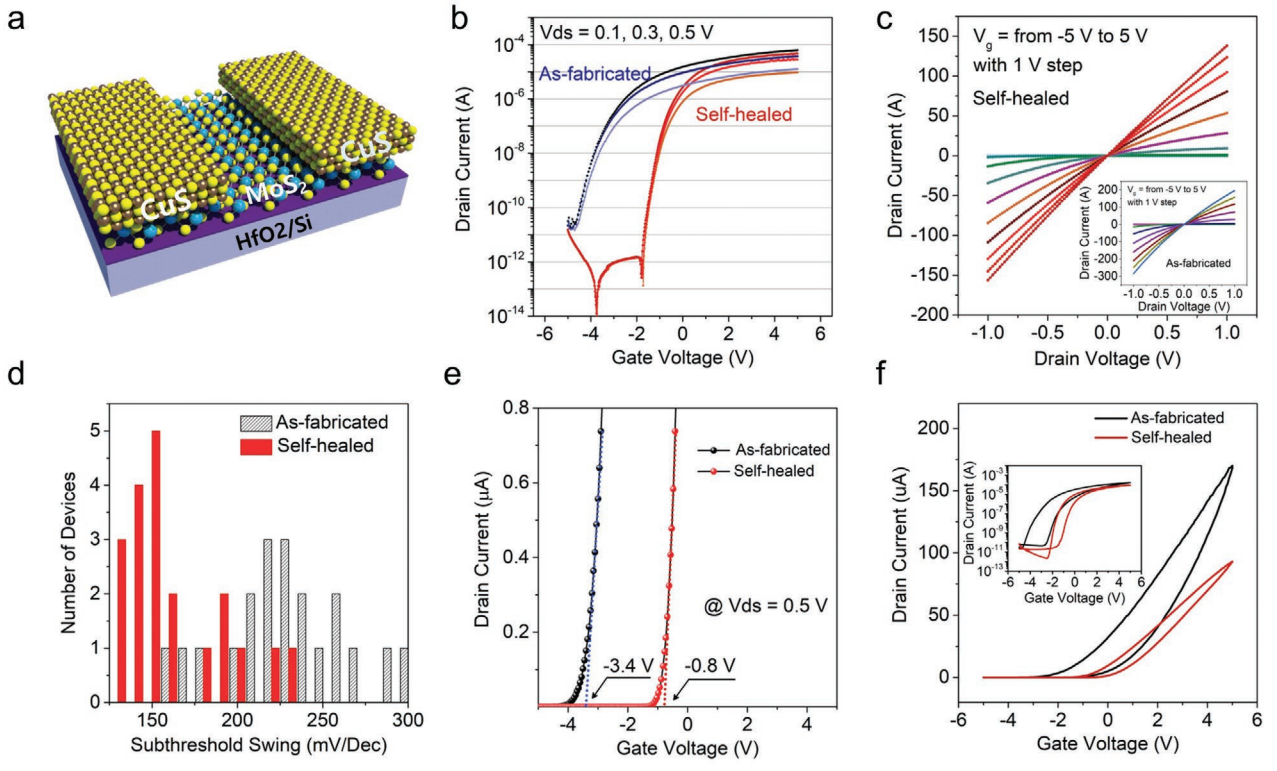

Figure 4. The MoS_2/CuS Transistor. a) Schematic illustration of the MoS_2/CuS transistor. b) Transfer curves at 0.1–0.5 V source-drain bias and c) output curves at different gate voltages (−5 to +5 V) of the as-fabricated and self-healed devices. Change in d) subthreshold swing values, e) threshold voltages, and f) hysteresis characteristics after mild thermal annealing to induce self-healing in MoS_2.

back-gated transistor configuration without any passivation layers. The improvement in the electrical properties of the self-healed devices can be attributed to the enhanced contact properties resulting from creation of chemically clean interface and reduction of unwanted Fermi-level pinning (see Figure S8, Supporting Information, for contact resistance measurement). The electrical properties of annealed CuS and MoS_2/CuS FET at 300 °C showed similar electrical properties (Figure S9, Supporting Information). The improvement in the mobility as well as subthreshold swing is a clear signature of the reduced defects and interface trap densities within the device channel and the interface.[29,33] Our MoS_2/CuS transistor showed impressive device performance (mobility, on/off ratio, and SS) and the values are the best reported so far among back-gated transistors with CVD-grown 1L-MoS_2, which is compared in Table S1, Supporting Information. Furthermore, the electrical properties of our device are significantly better than the device with copper contact and previously demonstrated vacancy-passivated devices (see Figure S10 and Table S2, Supporting Information, for comparison).

It is also evident that the threshold voltages were shifted toward positive voltages for the self-healed devices as shown in Figure 4e. At the drain voltage V_{ds} = 0.5 V, the threshold voltages were significantly changed from −3.4 V to −0.8 V, which were determined using a linear-extrapolation method, and the statistical charts, showing the shift of threshold voltages, are plotted in Figure S11, Supporting Information. We attribute such change in the threshold voltages to the SVSH in the MoS_2 channel, which shift fermi energy level toward the intrinsic level. To further elucidate that the shifts of threshold voltages are due to the SVSH in the MoS_2 channel, we also measured and compared the hysteresis behaviors of the as-fabricated and self-healed MoS_2/CuS FETs as shown in Figure 4e. A noticeable decrease in the hysteresis width was observed for the self-healed device compared to the as-fabricated device, which is a signature of reduced surface adsorbates due to the self-healed MoS_2 channel that are less energetically active to the adsorbates.[34]

The results presented thus far demonstrate the effect of the SVSH for the field-effect transistor applications. We now consider phototransistor performance of the self-healed MoS_2/CuS devices. It should be noted that defects can play as recombination centers during photodetection and impede efficient charge transport,[35,36] and the self-healed devices are expected to reach high photoresponsivity due to reduced scattering/recombination during photogenerated carrier transport/transfer from MoS_2 to CuS electrode. **Figure 5**a shows the transfer curve of the self-healed MoS_2/CuS phototransistor under various illumination intensities. The incident laser power density is estimated by considering the laser spot size (a diameter of 2 mm). Based on the measurement in Figure 5a, the photoresponsivity of the self-healed device is estimated using the equation $R = \frac{I_{Ph}}{P}$, where the I_{Ph} is the photocurrent and P is the

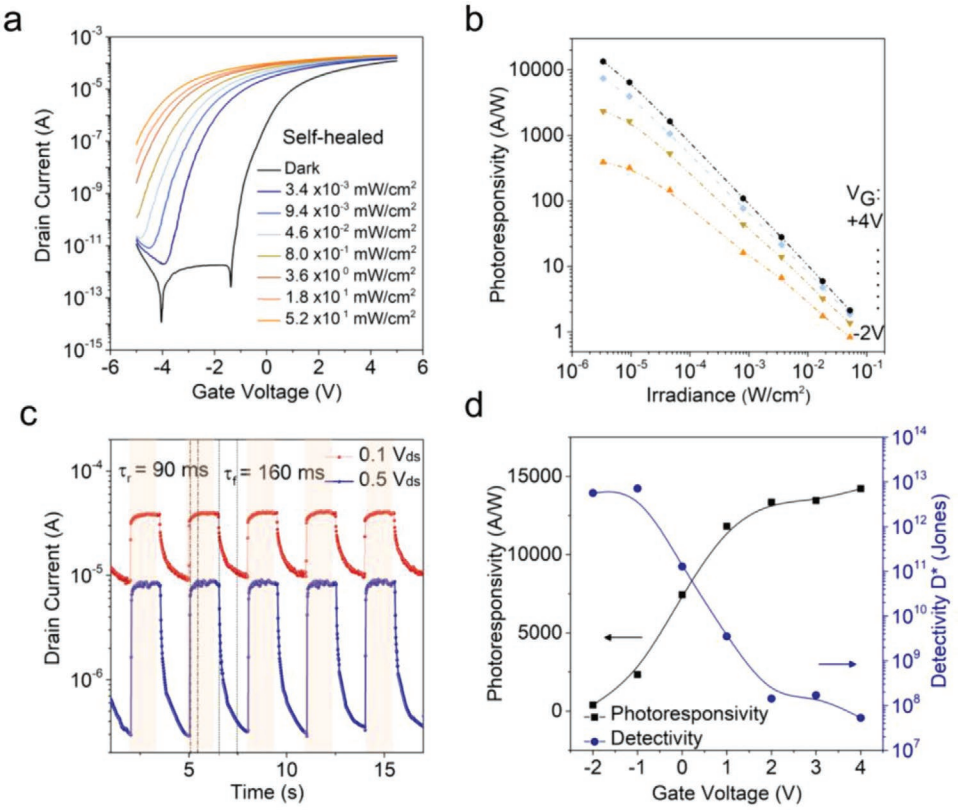

Figure 5. Phototransistor performance of the self-healed MoS_2/CuS Phototransistor. a) Measurements of drain current as a function of gate voltages under different incident laser power densities (dark to 52 mW cm^{-2}). b) Photoresponsivity as a function of incident laser power densities at different gate voltages (−2 to +4 V). c) Temporal response of photocurrent at drain voltages of 0.1 and 0.5 V. d) Photoresponsivity (primary-axis) and detectivity (secondary-axis) as a function of gate voltages.

incident laser power on the effective area of the devices. The photoresponsivity was plotted with respective to the incident laser power with varying gate voltages as shown in Figure 5b. We found that the photoresponsivity as high as $R = 13\,461.5$ A W^{-1} was calculated at $V_g = +4$ V and $P = 3.4 \times 10^{-3}$mW cm^{-2}. The dependence of photoresponsivity on the incident laser power follows a power law,[37] $R \approx P^{\alpha}$, where α is ranging from −0.76 to −0.92, which is higher than the values reported by other 2D based photosensors[37–39] and is close to the saturation factor $\alpha = -1$. Specifically, the non-unity exponent generally involves defect sites,[35] and the high α value suggests that the MoS_2/CuS phototransistor has less defects by the SVSH.

Figure 5c shows the stable and repeated temporal response of the self-healed device after switching the 450 nm laser illumination on and off for 3 s under applied bias voltages of $V_{ds} = 0.1$ V and 0.5 V and $V_g = 0$ V. A fast rise and decay time of 90 ms and 160 ms, respectively, were observed for the MoS_2/CuS device. We further tested the phototransistor performance by measuring and plotting photoresponsivity and specific detectivity, D^*, with respective to the back-gate voltages as shown in Figure 5d. The high photoresponsivity under the positive polarity back gate voltages can be attributed to the lower contact resistance which effectively propagate charges into the MoS_2 channel.[40] The D^* was also found to be dependent on the back-gate voltages (see Figure S12, Supporting Information, for detectivity and NEP calculation).[36,41,42] While R reached the highest value under the positive polarity gate voltage, D^* was increased up to 10^{13} jones under the negative polarity gate voltage due to the significantly reduced dark current, and the values are among the highest reported performance for pristine MoS_2-based photodetectors as summarized in Table S3, Supporting Information.

The attractive features of the 2D MoS_2 channel and ultrathin CuS electrodes in terms of their outstanding electrical properties and their flexibility enable us to explore new avenues for developing flexible optoelectronics based on those 2D materials. The ultrathin CuS electrode not only induce self-healing in MoS_2, but also possess excellent electrical properties and outstanding stability under mechanical strain, thus making them highly suitable for flexible applications. In order to address the feasibility of our self-healed MoS_2/CuS device in flexible device applications, we have designed and fabricated a simple two-terminal flexible MoS_2 photodetector on a flexible Polyethylene terephthalate (PET) substrate, and the resulting device image is shown in **Figure 6**a. The drain source-current versus drain-source voltage under varying illumination intensities is plotted in a logarithmic scale in Figure 6b. It can be seen that the flexible MoS_2/CuS device shows the symmetric, ohmic contacts and current modulation under the 450 nm laser illumination. Based on the measured data, the photoresponsivity, R, was

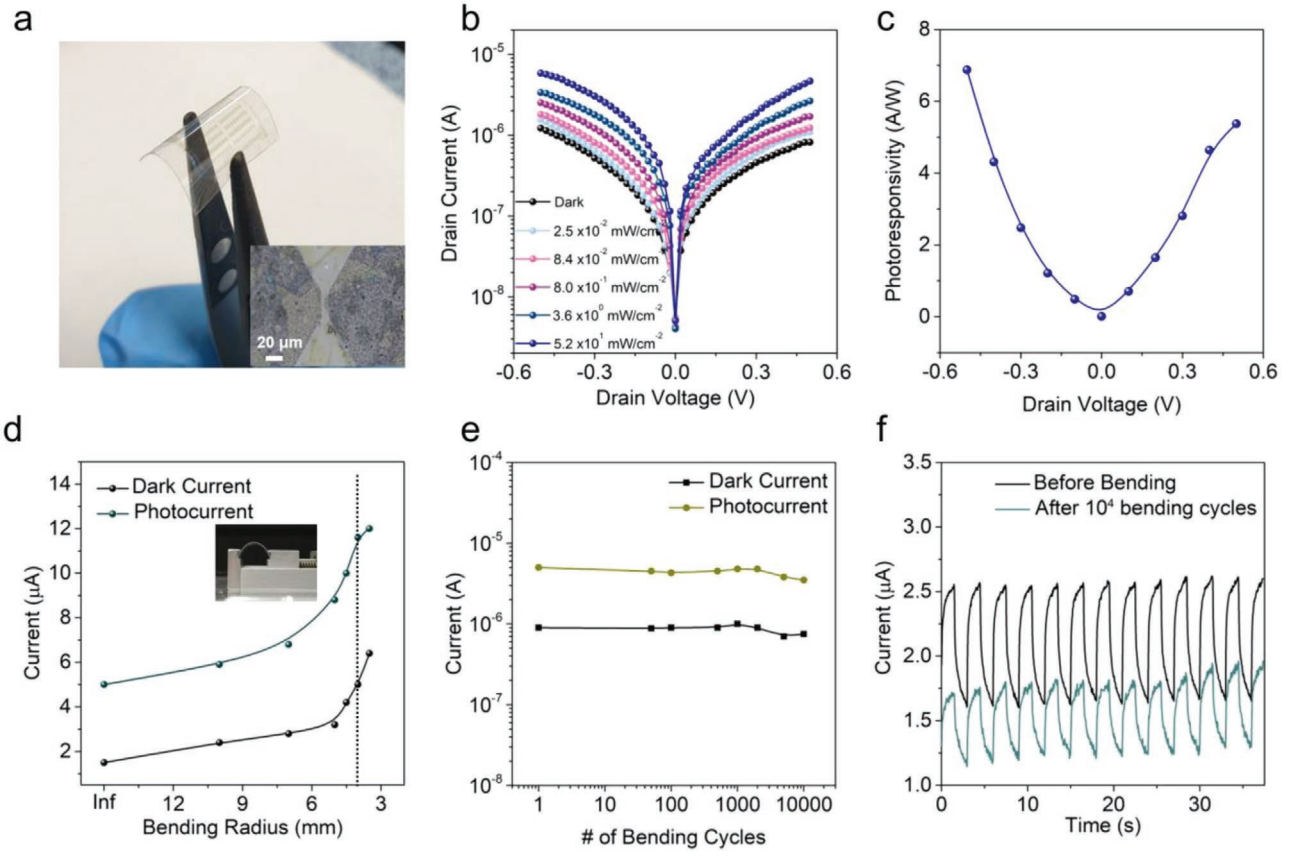

Figure 6. Flexible MoS_2/CuS Photodetector. a) Optical image of the two-terminal MoS_2/CuS flexible device. b) The *IV*-curves of the MoS_2/CuS photodetector at varying illumination intensities. c) Photoresponsivity as a function of applied drain voltages. The change in dark current and photocurrent measured with respect to d) bending radius and e) bending cycles. f) Temporal photocurrent measurement after 10^4 bending cycles.

reached up to 7 A W^{-1} when it was calculated with respective to the applied voltages as shown in Figure 6c.

To further investigate and characterize the MoS_2/CuS flexible photodetector, we have performed in situ bending photoresponse measurements as shown in Figure 6d. The inset image of Figure 6d shows our bespoke bending machine employed to apply strain on the photodetector. Along with the changes in the dark current, the photocurrent was increased as the bending radius decreases down to 3.5 mm. Such trend observed for the flexible MoS_2/CuS photodetector under bending strain is consistent with the previous report showing piezoresistive effect,[43] where the contact barrier height is reduced due to the changes in the electron affinity under the applied tensile strain and the corresponding photo-electrical properties are improved due to the reduced contact barriers.

To investigate mechanical stability of our MoS_2/CuS flexible photodetector, we have monitored the change in the dark current and photocurrent in terms of the number of bending cycles at a bending radius of 4 mm. As shown in Figure 6e, the photocurrent and dark current was well maintained with only a slight variation in the magnitude even the device was bent up to 10^4 cycles, and the time domain photocurrent was measured to shown the stability of our MoS_2/CuS flexible photodetector before and after the bending tests as shown in Figure 6f. Such high stability of our MoS_2/CuS flexible photodetector under mechanical bending tests is strongly attributed to the ultrathin nature of CuS electrodes as well as high young's modulus of MoS_2 monolayer, all of which are highly suitable for next-generation flexible optoelectronic device applications.

3. Conclusion

In conclusion, we have developed the innovative self-healed sulfide-electrode system for 2D MoS_2 devices that showed impressive transistor and phototransistor performance. We have shown that mild thermal annealing in the CuS/MoS_2 heterogenous structure induces excess sulfur adatoms to heal the defect sites of MoS_2 monolayer, as known as sulfur vacancy self-healing, which in turn improves contact and MoS_2 channel properties. The self-healed, back-gated transistors and phototransistors showed high mobility up to 97.6 cm^2 $(Vs)^{-1}$, low subthreshold swing of 120 mV per decade, high photoresponsivity up to 13 461.5 A W^{-1}, and detectivity up to 10^{13} jones without any passivation layers. We further demonstrated the flexible photodetector based on the CuS electrodes and MoS_2 channel and proved the outstanding mechanical stability under the multiple bending test. We believe that our device integration approaches should pave a new way of designing (opto)electronics based on 2D TMDC materials and CuS electrode.

4. Experimental Section

Synthesis of Monolayer MoS_2 and CuS Nanosheet: Monolayer MoS_2 was grown on a 300 nm SiO_2/Si substrate using a thermal CVD method and thermodynamically stable synthesis.[44,45] The growth was carried in a 2 in. quartz tube by placing 0.05 mg of MoO_3 precursor (Sigma-Aldrich, >99%) and 50 mg of sulfur powder (Sigma-Aldrich, >99.98%) which was placed upstream of the furnace. The growth was carried at 750–800 °C for 5–10 min. CuS nanosheet was synthesized by exposing the Cu film to ammonium sulfide (Alfa Aesar, 20–24% aqueous solution). Cu film was deposited using a thermal evaporator.

Fabrication of MoS_2 and CuS Nanosheet Heterostructure: The electrode pad for the CuS electrodes were patterned using a standard photolithography process. To transfer MoS_2 monolayers and CuS electrodes, polystyrene (PS) film was used as the transferring medium.[21] MoS_2 and CuS electrodes were spin coated with PS ($M_W \approx$ 192 000) film. During the transfer process, the PS film held MoS_2 and CuS layers, while water penetrated between the PS film and the substrate for detachment. The detached PS film with MoS_2 or CuS was dried in air and transferred onto the targeting substrate (SiO_2, HfO_2, and PET substrate). The PS film was removed by dipping the substrate in toluene for 24 h. For the preparation of the XPS sample, large area and fully covered MoS_2 film (>5 mm × 5 mm) was transferred on CuS film (>5 mm × 5mm) which was synthesized on SiO_2/Si substrate. The fabricated MoS_2/CuS heterostructure was annealed at 150 °C under vacuum condition.

Characterization of MoS_2 and CuS: The Raman and PL measurements were carried out using 532 nm laser on Alpha 300 R confocal Raman spectroscopy. KPFM images were obtained using a commercial AFM setup (Park Systems, XE7) with a lock-in amplified (SR-830, Stanford Research Systems). For KPFM measurement, Cr/Au-coated Si tip (NSC14) was used. The tip was calibrated with highly oriented pyrolytic graphite (HOPG) before KPFM measurement.

Electrical and Optoelectrical Measurement: (Opto)electrical properties were measured using the semiconductor characterization system (4200A-SCS, Keithley), Tektronix MDO3054 oscilloscope, Stanford Research Systems SR570 current preamplifier, and MS Tech probe station. Strain-dependent photocurrent measurement was carried out using our bespoke bending machine and bending machine motorized system (ST-BJS-0810-SSU) for the bending cycle tests. 450 nm laser diode (MDL-III-450L) was used to measure the photoresponse of MoS_2/CuS devices.

DFT Calculations: The atomic geometries and sulfur adatom binding energies of the various MoS_2 surface structures were calculated using the Vienna ab initio simulation package (VASP).[46,47] The exchange–correlation functional was approximated using the Perdew–Burke–Ernzerhof (PBE) expression.[48] In order to account for weak van der Waals (vdW) interactions between sulfur adatom and MoS_2 surfaces, the optB86b-vdW functional, implemented in VASP by Klimeš et al., was used for all of the binding energy calculations.[49] Electron–ion interactions were modeled using the projector augmented wave (PAW) method.[50] The electronic wave functions were expanded in a basis set of plane waves with a kinetic energy cutoff of 500 eV. The geometry relaxation step was repeated until the ionic forces were reduced to below 0.01 eV $Å^{-1}$. The k-space integration step was performed with finite sampling of the k-points on a 6 × 6 × 1 mesh in the Brillouin zone to optimize the geometry of each modeled structure. To minimize the interactions between neighboring image cells, vacuum regions at least 23 Å in length along the direction (z) perpendicular to the 2D surface were included. For the BES calculation of the sulfur adatom, atomic geometry optimizations of five MoS_2 model surfaces, specifically those of perfect MoS_2 surface and four defective MoS_2 surfaces with $1V_S$ or $2V_S$ or $2V_{2S}$ or $1V_S$ and $1S_A$ (per unit-cell), were performed preferentially. All MoS_2 model surface systems were fully relaxed. After that, for the relaxed perfect and defective MoS_2 surface structures obtained from the prior calculation, the overall molybdenum atoms were fixed during the geometry optimization of the sulfur adatom adsorbed on the various model surfaces to maintain the original structures of the pre-relaxed MoS_2 surfaces. Also, the x and y positions of the sulfur adatom were fixed, and only its z position was relaxed.

Supporting Information

Supporting Information is available from the Wiley Online Library or from the author.

Acknowledgements

S.P. and S.J. contributed equally to this work. This work was supported by the National Research Foundation (NRF) of Korea (2019R1A2C1005930). This work was also supported by a project from the Korea Research Institute of Chemical Technology (KRICT) (grant no. SI2151-10).

Note: The format of the Data Availability Statement was updated on October 12, 2021 after initial publication online.

Conflict of Interest

The authors declare no conflict of interest.

Data Availability Statement

The data that support the findings of this study are available from the corresponding author upon reasonable request.

Keywords

flexible photodetector, high mobility transistor, low subthreshold swing, MoS_2, self-healing, ultrasensitive photodetection

Received: March 16, 2021
Revised: July 27, 2021
Published online: September 4, 2021

[1] J. Lee, S. Pak, Y.-W. Lee, Y. Cho, J. Hong, P. Giraud, H. S. Shin, S. M. Morris, J. I. Sohn, S. Cha, J. M. Kim, *Nat. Commun.* **2017**, *8*, 14734.
[2] S. Pak, J. Lee, Y.-W. Lee, A.-R. Jang, S. Ahn, K. Y. Ma, Y. Cho, J. Hong, S. Lee, H. Y. Jeong, H. Im, H. S. Shin, S. M. Morris, S. Cha, J. I. Sohn, J. M. Kim, *Nano Lett.* **2017**, *17*, 5634.
[3] S. Pak, A. R. Jang, J. Lee, J. Hong, P. Giraud, S. Lee, Y. Cho, G. H. An, Y. W. Lee, H. S. Shin, S. M. Morris, S. Cha, J. I. Sohn, J. M. Kim, *Nanoscale* **2019**, *11*, 4726.
[4] J. Wang, Q. Yao, C. W. Huang, X. Zou, L. Liao, S. Chen, Z. Fan, K. Zhang, W. Wu, X. Xiao, C. Jiang, W. W. Wu, *Adv. Mater.* **2016**, *28*, 8302.
[5] Y. Yoon, K. Ganapathi, S. Salahuddin, *Nano Lett.* **2011**, *11*, 3768.
[6] K. Kaasbjerg, K. S. Thygesen, K. W. Jacobsen, *Phys. Rev. B* **2012**, *85*, 115317.
[7] Y. Liu, H. Wu, H. C. Cheng, S. Yang, E. B. Zhu, Q. Y. He, M. N. Ding, D. H. Li, J. Guo, N. O. Weiss, Y. Huang, X. F. Duan, *Nano Lett.* **2015**, *15*, 3030.
[8] Y. Liu, J. Guo, E. B. Zhu, L. Liao, S. J. Lee, M. N. Ding, I. Shakir, V. Gambin, Y. Huang, X. F. Duan, *Nature* **2018**, *557*, 696.
[9] H. J. Chuang, B. Chamlagain, M. Koehler, M. M. Perera, J. Q. Yan, D. Mandrus, D. Tomanek, Z. X. Zhou, *Nano Lett.* **2016**, *16*, 1896.
[10] Y. Wang, J. C. Kim, R. J. Wu, J. Martinez, X. J. Song, J. Yang, F. Zhao, K. A. Mkhoyan, H. Y. Jeong, M. Chhowalla, *Nature* **2019**, *568*, 70.
[11] R. Kappera, D. Voiry, S. Yalcin, B. Branch, G. Gupta, A. Mohite, M. Chhowalla, *Nat. Mater.* **2014**, *13*, 1128.
[12] A. M. van der Zande, P. Y. Huang, D. A. Chenet, T. C. Berkelbach, Y. You, G. H. Lee, T. F. Heinz, D. R. Reichman, D. A. Muller, J. C. Hone, *Nat. Mater.* **2013**, *12*, 554.
[13] Y. J. Zhan, Z. Liu, S. Najmaei, P. M. Ajayan, J. Lou, *Small* **2012**, *8*, 966.
[14] W. Park, J. Baik, T. Y. Kim, K. Cho, W. K. Hong, H. J. Shin, T. Lee, *ACS Nano* **2014**, *8*, 4961.
[15] Z. F. Zhang, X. L. Xu, J. Song, Q. G. Gao, S. C. Li, Q. L. Hu, X. F. Li, Y. Q. Wu, *Appl. Phys. Lett.* **2018**, *113*, 202103.
[16] H. Kwon, S. Garg, J. H. Park, Y. Jeong, S. Yu, S. M. Kim, P. Kung, S. Im, *NPJ 2D Mater. Appl.* **2019**, *3*, 9.
[17] T. Y. Kim, M. Amani, G. H. Ahn, Y. Song, A. Javey, S. Chung, T. Lee, *ACS Nano* **2016**, *10*, 2819.
[18] S. Pak, J. Lim, J. Hong, S. Cha, *Catalysts* **2021**, *11*, 70.
[19] J. Hong, B. S. Kim, B. Hou, S. Pak, T. Kim, A. R. Jang, Y. Cho, S. Lee, G. H. An, J. E. Jang, S. M. Morris, J. I. Sohn, S. Cha, *ACS Appl. Mater. Interfaces* **2021**, *13*, 4244.
[20] A. Gurarslan, Y. F. Yu, L. Q. Su, Y. L. Yu, F. Suarez, S. Yao, Y. Zhu, M. Ozturk, Y. Zhang, L. Y. Cao, *ACS Nano* **2014**, *8*, 11522.
[21] S. W. Jung, S. Pak, S. Lee, S. Reimers, S. Mukherjee, P. Dudin, T. K. Kim, M. Cattelan, N. Fox, S. S. Dhesi, C. Cacho, S. Cha, *Appl. Surf. Sci.* **2020**, *532*, 147390.
[22] X. K. Zhang, Q. L. Liao, S. Liu, Z. Kang, Z. Zhang, J. L. Du, F. Li, S. H. Zhang, J. K. Xiao, B. S. Liu, Y. Ou, X. Z. Liu, L. Gu, Y. Zhang, *Nat. Commun.* **2017**, *8*, 15881.
[23] Y. Wang, L. Qi, L. Shen, Y. H. Wu, *J. Appl. Phys.* **2016**, *119*, 154301.
[24] H. V. Han, A. Y. Lu, L. S. Lu, J. K. Huang, H. N. Li, C. L. Hsu, Y. C. Lin, M. H. Chiu, K. Suenaga, C. W. Chu, H. C. Kuo, W. H. Chang, L. J. Li, Y. M. Shi, *ACS Nano* **2016**, *10*, 1454.
[25] M. Amani, D.-H. Lien, D. Kiriya, J. Xiao, A. Azcatl, J. Noh, S. R. Madhvapathy, R. Addou, K. C. Santosh, M. Dubey, K. Cho, R. M. Wallace, S.-C. Lee, J.-H. He, J. W. Ager, X. Zhang, E. Yablonovitch, A. Javey, *Science* **2015**, *350*, 1065.
[26] S. Roy, W. Choi, S. Jeon, D. H. Kim, H. Kim, S. J. Yun, Y. Lee, J. Lee, Y. M. Kim, J. Kim, *Nano Lett.* **2018**, *18*, 4523.
[27] H.-V. Han, A.-Y. Lu, L.-S. Lu, J.-K. Huang, H. Li, C.-L. Hsu, Y.-C. Lin, M.-H. Chiu, K. Suenaga, C.-W. Chu, H.-C. Kuo, W.-H. Chang, L.-J. Li, Y. Shi, *ACS Nano* **2016**, *10*, 1454.
[28] H. Li, C. Tsai, A. Koh, L. Cai, A. W. Contryman, A. H. Fragapane, J. Zhao, H. Han, H. C. Manoharan, F. Abild-Pedersen, J. K. Nørskov, X. Zheng, *Nat. Mater.* **2015**, *15*, 48.
[29] S. Bhattacharjee, K. L. Ganapathi, D. N. Nath, N. Bhat, *IEEE Trans. Electron Devices* **2016**, *63*, 2556.
[30] A. Allain, J. H. Kang, K. Banerjee, A. Kis, *Nat. Mater.* **2015**, *14*, 1195.
[31] S. Choi, Z. Shaolin, W. Yang, *J. Korean Phys. Soc.* **2014**, *64*, 1550.
[32] J. Peto, T. Ollar, P. Vancso, Z. I. Popov, G. Z. Magda, G. Dobrik, C. Y. Hwang, P. B. Sorokin, L. Tapaszto, *Nat. Chem.* **2018**, *10*, 1246.
[33] F. Giannazzo, G. Fisichella, A. Piazza, S. Di Franco, G. Greco, S. Agnello, F. Roccaforte, *Phys. Status Solidi RRL* **2016**, *10*, 797.
[34] L. Qi, Y. Wang, L. Shen, Y. Wu, *Appl. Phys. Lett.* **2016**, *108*, 063103.
[35] W. Zhang, J.-K. Huang, C.-H. Chen, Y.-H. Chang, Y.-J. Cheng, L.-J. Li, *Adv. Mater.* **2013**, *25*, 3456.
[36] D. Kufer, G. Konstantatos, *Nano Lett.* **2015**, *15*, 7307.
[37] B. K. Sarker, E. Cazalas, T. F. Chung, I. Childres, I. Jovanovic, Y. P. Chen, *Nat. Nanotechnol.* **2017**, *12*, 668.
[38] M. Buscema, D. J. Groenendijk, S. I. Blanter, G. A. Steele, H. S. J. van der Zant, A. Castellanos-Gomez, *Nano Lett.* **2014**, *14*, 3347.
[39] Q. H. Zhao, W. Wang, F. Carrascoso-Plana, W. Q. Jie, T. Wang, A. Castellanos-Gomez, R. Frisenda, *Mater. Horiz.* **2020**, *7*, 252.
[40] S. Pak, Y. Cho, J. Hong, J. Lee, S. Lee, B. Hou, G. H. An, Y. W. Lee, J. E. Jang, H. Im, S. M. Morris, J. I. Sohn, S. Cha, J. M. Kim, *ACS Appl. Mater. Interfaces* **2018**, *10*, 38264.
[41] Y. J. Fang, A. Armin, P. Meredith, J. S. Huang, *Nat. Photonics* **2019**, *13*, 1.
[42] G. Konstantatos, J. Clifford, L. Levina, E. H. Sargent, *Nat. Photonics* **2007**, *1*, 531.
[43] S. Pak, J. Lee, A. R. Jang, S. Kim, K.-H. Park, J. I. Sohn, S. Cha, *Adv. Funct. Mater.* **2020**, *30*, 2002023.
[44] J. Lee, S. Pak, P. Giraud, Y. W. Lee, Y. Cho, J. Hong, A. R. Jang, H. S. Chung, W. K. Hong, H. Jeong, H. Shin, L. G. Occhipinti, S. M. Morris, S. Cha, J. Sohn, J. Kim, *Adv. Mater.* **2017**, *29*, 1702206.

[45] J. Lee, S. Pak, Y. W. Lee, Y. Park, A. R. Jang, J. Hong, Y. Cho, B. Hou, S. Lee, H. Y. Jeong, H. S. Shin, S. M. Morris, S. Cha, J. I. Sohn, J. M. Kim, *ACS Nano* **2019**, *13*, 13047.
[46] G. Kresse, *J. Non-Cryst. Solids* **1995**, *193*, 222.
[47] G. Kresse, J. Furthmuller, *Phys. Rev. B* **1996**, *54*, 11169.
[48] J. P. Perdew, K. Burke, M. Ernzerhof, *Phys. Rev. Lett.* **1996**, *77*, 3865.
[49] J. Klimes, D. R. Bowler, A. Michaelides, *J. Phys.: Condens. Mater.* **2010**, *22*, 022201.
[50] P. E. Blochl, *Phys. Rev. B* **1994**, *50*, 17953.